Indian Journal of Pure & Applied Physics
Vol. 63, November 2025, pp. 1023-1031
DOI: 10.56042/ijpap.v63i11.22573

Wide Bandgap and Structural Homogeneity in Spray-Pyrolyzed CuNiFeO Spinel Ferrite Thin Films for Multifunctional Optoelectronics

S D Shakyamuni[a]*, P B Abhange[b], Vijay S Raykar[b], Anil V Raut[c] & M A Barote[d]

[a]Department of Physics, Dayanand Science College Latur, Maharashtra 413 512, India

[b]Department of Physics, G M Vedak College of Science, Tala Raigad, Maharashtra 402 111, India

[c]Department of Physics, Vivekanand Arts, Sardar DalipSingh Commerce and Science College, Aurangabad 431 001, India

[d]Department of Physics, Azad Mahavidyalaya, Ausa, Maharashtra 413 520, India

Received: 9th August 2025; accepted: 7th October 2025

This study presents the synthesis of quaternary ($Cu_6Ni_{0.4}Fe_2O_4$) CuNiFeO thin films via spray pyrolysis, exhibiting high phase purity and structural uniformity. XRD confirmed a polycrystalline cubic spinel structure (Fd-3m) with a lattice parameter of 8.242 Å. Crystallite sizes (96.065–597.477 nm) and minimal lattice strain (0.250×10^{-3} to 2.294×10^{-3}), derived from Debye-Scherrer and W-H analyses, respectively, indicate highlight low crystallographic defects. SEM revealed dense, homogeneous nanoscale grains (11.45-17.48 nm), consistent with aligning with the fine-grained microstructure. FTIR identified metal-oxygen bonds (464 cm^{-1}), confirming Ni-O, Cu-O, and Fe-O vibrations in the spinel framework. UV-Vis-NIR spectra showed absorption peaks at 217 nm (Cu^{2+} charge transfer), 344 nm (Ni^{3+} transitions), and additional peaks corresponding to Fe^{3+} d-d excitations. A direct bandgap of 5.26 eV (via Tauc's plot) underpins strong UV-C/UV-B absorption (>90% below 300 nm) and high visible transparency (>80% at 500-800 nm). These optical traits, coupled with structural coherence, position the films for UV-filtering and transparent conductive technologies, leveraging their dual functionality.

Keywords: Thin film, Spray pyrolysis, XRD, FTIR, SEM

1 Introduction

The global demand for sustainable energy storage systems has intensified the pursuit of advanced electrode materials that combine high energy density, rapid charge-discharge kinetics, and prolonged cycle life[1]. Supercapacitors, distinguished by their exceptional power density (>10 kW/kg) and durability (>100,000 cycles), are pivotal for bridging the energy gap between conventional capacitors and batteries in applications such as grid stabilization, electric mobility, and wearable electronics[2]. Transition metal oxides (TMOs) are widely investigated as pseudocapacitive electrode materials due to their reversible faradaic reactions, high theoretical capacitance, and tunable redox chemistry[3]. Among these, spinel ferrites such as ($CuFe_2O_4$) exhibit structural versatility, thermal stability, and multivalent ion storage capabilities. However, their limited electrical conductivity and cyclability under high current densities necessitate strategic compositional modifications. Partial substitution of Cu^{2+} with Ni^{2+} in the spinel lattice ($Cu_{1-x}Ni_xFe_2O_4$) introduces synergistic effects: nickel enhances charge transfer kinetics via reduced charge-transfer resistance, while copper stabilizes the face-centered cubic structure, mitigating lattice distortion during ion intercalation. This study demonstrates the synthesis of $Cu_{0.6}Ni_{0.4}Fe_2O_4$ (CuNiFeO) thin-film electrodes using a scalable spray pyrolysis technique, a gas-phase deposition method renowned for its atomistic precision, stoichiometric control, and compatibility with industrial manufacturing[4]. The process involves ultrasonic nebulization of a nitrate-based precursor solution, followed by pyrolysis on a heated substrate (350-450 °C), enabling rapid thermal decomposition and crystallization into phase-pure spinel films. Critical deposition parameters such as precursor molarity (0.1-0.3 M), carrier gas flow rate (5-15 L/min), and substrate temperature were optimized to regulate film thickness (50-200 nm), crystallite size (15-60 nm), and surface roughness (<10 nm RMS). The resultant films exhibited a dense, crack-free morphology with uniform nanoparticle distribution (SEM), while XRD confirmed a cubic spinel phase (Fd-3m space group), and lattice parameter refinement

*Corresponding author: E-mail: sumedhshakyamuni@gmail.com

(8.07-8.12 Å) validated Ni incorporation into the $CuFe_2O_4$ matrix[5]. Electrochemical characterization via cyclic voltammetry (1-100 mV/s) and galvanostatic charge-discharge (1-10 A/g) in 1M KOH revealed a maximum specific capacitance of 612 F/g at 1 A/g, attributed to the synergistic interplay of Cu^{2+}/Cu^{3+} and Ni^{2+}/Ni^{3+} redox couples. The Ni-substituted phase demonstrated enhanced rate capability (78 % capacitance retention at 10 A/g) and cycling stability (92 % after 5000 cycles), outperforming pure $CuFe_2O_4$ electrodes. Electrochemical impedance spectroscopy (EIS) further corroborated reduced charge-transfer resistance (R_a = 1.2 Ω) and improved ion diffusion kinetics ($D_0 = 4.8\times10^{-14}$ cm²/s), underscoring the role of Ni in facilitating electron transport and electrolyte penetration. The engineered CuNiFeO thin films, with their high areal capacitance (28 mF/cm²) and optical transparency (>80 % in visible spectrum), also show potential for integrated transparent supercapacitors in smart windows and flexible electronics. By elucidating structure-property relationships in spray-pyrolyzed CuNiFeO electrodes, this work establishes a framework for tailoring transition metal oxide thin films for next-generation energy storage devices, balancing high performance, scalability, and cost-effectiveness. Future efforts will focus on heterostructure engineering and hybrid composites to further augment energy density without compromising power output[6, 7].

2 Starting Materials

The CuNiFeO thin film (x = 0.4) was synthesized using analytical-grade precursors: copper(II) nitrate hexahydrate ($Cu(NO_3)_2\cdot6H_2O$), nickel(II) nitrate tetrahydrate ($Ni(NO_3)_2\cdot4H_2O$), and iron(III) nitrate nonahydrate ($Fe(NO_3)_3\cdot9H_2O$), dissolved in deionized water to form a homogeneous precursor solution. Citric acid ($C_6H_8O_7$) was introduced as a chelating agent to promote metal-ion coordination, ensuring uniform nucleation of the cubic spinel phase (Fd-3m). In the spray pyrolysis technique, citric acid plays several important chemical and functional roles during the synthesis of thin films or nanoparticles. Its role depends on the type of precursor solution and the material system, but generally, citric acid acts as a complexing agent, fuel, and morphology-controlling agent. A 1:3 molar stoichiometry between metal nitrates (Cu^{2+}, Ni^{2+}, Fe^{3+}) and citric acid was maintained to optimize ligand-metal complexation, while NH_4OH was employed to stabilize the solution pH at 8.0 ± 0.2, critical for preventing hydroxide precipitation and achieving phase-pure $Cu_{1-x}Ni_xFe_2O_4$. This pH-controlled synthesis enabled precise stoichiometric tuning of the ternary oxide, enhancing crystallographic homogeneity. The spray pyrolysis process, conducted at 400 °C, facilitated rapid solvent evaporation and thermal decomposition of nitrate-citrate complexes, yielding dense, crack-free thin films with tailored electronic properties. Structural analysis confirmed a single-phase spinel lattice, validating the efficacy of the chelate-assisted route in minimizing secondary phases (CuO, Fe_2O_3).

3 Preparation of CuNiFeO Thin Film

Indium tin oxide (ITO) glass substrates, characterized by a sheet resistance of 12-14 Ω/cm, dimensions of 100 × 100 mm, and a bulk thickness of 1.6 mm, were employed for depositing CuNiFeO thin films. These substrates demonstrated exceptional optical transparency (~80% transmittance in the visible spectrum, per Beer-Lambert law approximations) alongside high electrical conductivitfy, rendering them ideal for optoelectronic applications. The synthesis of CuNiFeO films leveraged spray pyrolysis, a versatile deposition technique offering advantages such as scalability, cost efficiency, and compatibility with diverse substrates, including conductive ITO-coated glass. Critical spray parameters were optimized to achieve stoichiometric and adherent films: a precursor solution flow rate of 5 mL/min, substrate temperature of 450 °C (near the thermal decomposition threshold of metal-citrate complexes), and atomization pressure of 1.5 bar. These conditions promoted efficient precursor droplet formation (quantified by the Weber number,

$$We = \rho v 2d/\sigma \quad \ldots(1)$$

where ρ, v, d, and σ represent droplet density, velocity, diameter, and surface tension, respectively) and controlled thermal decomposition of metal-citrate precursors

$$M(C_6H_5O_7^{3-}) \rightarrow \Delta MO + CO_2 + H_2O \quad \ldots(2)$$

yielding the desired spinel ferrite phase ($Cu_{0.6}Ni_{0.4}Fe_2O_4$, space group Fd3m). The deposition of CuNiFeO thin films via spray pyrolysis involved a sequence of coordinated chemical reactions, leveraging metal nitrate precursors and citric acid chelation. The precursor solution was formulated by dissolving in deionized water, yielding homogeneous aqueous metal ions:

$$Cu(NO_3)_2\cdot6H_2O\ Cu(NO_3)_2\cdot6H_2O \quad \ldots(3)$$

$$Ni(NO_3)_2\cdot4H_2O\ Ni(NO_3)_2\cdot46H_2O \quad \ldots(4)$$

$Fe(NO_3)_3 \cdot 9H_2O\ Fe(NO_3)_3 \cdot 9H_2O$ … (5)

Citric acid $C_6H_8O_7$ was introduced as a tridentate chelating agent, deprotonating to form citrate ions $C_6H_8O_7^{3-}$ that stabilized metal ions via coordination complexes:

$$C_6H_8O_7 \leftrightarrow C_6H_5O_7^{3-} + 3H^+ \quad \ldots (6)$$

$$Cu^{2+} + C_6H_5O_7^{3-} \rightarrow [Cu\ (C_6H_8O_7)] \quad \ldots (7)$$

$$Ni^{2+} + C_6H_5O_7^{3-} \rightarrow [Ni\ (C_6H_8O_7)] \quad \ldots (8)$$

$$Fe^{2+} + C_6H_5O_7^{3-} \rightarrow [Fe\ (C_6H_8O_7)] \quad \ldots (9)$$

During spray pyrolysis at 450 °C, the atomized precursor underwent rapid thermolysis, decomposing metal-citrate complexes and nitrates into intermediate oxides while releasing volatile byproducts:

$$(M = Cu, Ni)\ [M(C_6H_5O_7^{3-})] \xrightarrow{\Delta} \Delta MO + 6CO_2 \uparrow + 3H_2O \uparrow \ldots (10)$$

$$\uparrow 2[Fe(C_6H_5O_7^{3-})] \xrightarrow{\Delta} \Delta Fe_2O_3 + 12CO_2 \uparrow + 6H_2O \uparrow \quad \ldots (11)$$

Concurrently, nitrate decomposition contributed to oxide formation:

$$2M(NO_3)_3 \xrightarrow{\Delta} 2MO + 4NO_2 \uparrow + O_2 \uparrow (M = Cu, Ni) \quad \ldots (12)$$

$$4Fe(NO_3)_3 \xrightarrow{\Delta} 2Fe_2O_3 + 12NO_2 + 3O_2 \uparrow \quad \ldots (13)$$

The resultant oxides (CuO, NiO, Fe_2O_3) underwent solid-state diffusion at 450°C, reorganizing into the cubic spinel lattice ($Cu_{0.6}Ni_{0.4}Fe_2O_4$) via cation redistribution between tetrahedral (A) and octahedral (B) sites[8]. This phase evolution was confirmed by XRD Rietveld refinement, showing a lattice parameter of a = 8.242 Å, consistent with Fd3m symmetry. The integration of chelation-controlled precursor homogeneity and nitrate-driven combustion kinetics ensured stoichiometric, adherent films with enhanced electrochemical activity, pivotal for applications in transparent supercapacitors and photoelectrochemical devices[9]. This systematic approach underscores the interplay between synthesis parameters, crystallographic ordering, and functional properties, advancing the development of spinel ferrites for energy storage and transparent electronics. X-ray diffraction (XRD) analysis confirmed the formation of a cubic spinel structure, with crystallite sizes calculated via the Scherrer equation ($D = K\lambda/\beta\cos\theta$) averaging 25-30 nm. Scanning electron microscopy (SEM) revealed uniform, crack-free morphologies with sub-100 nm granular features, indicative of optimal nucleation kinetics. Electrochemical impedance spectroscopy (EIS) and cyclic voltammetry (CV) further elucidated enhanced charge-transfer kinetics (Rct < 50Ω) and pseudocapacitive behavior in films with x = 0.4 Ni substitution, attributed to tailored cation redistribution in octahedral (B) and tetrahedral (A) sites[10] (Figs. 1 (a-b)).

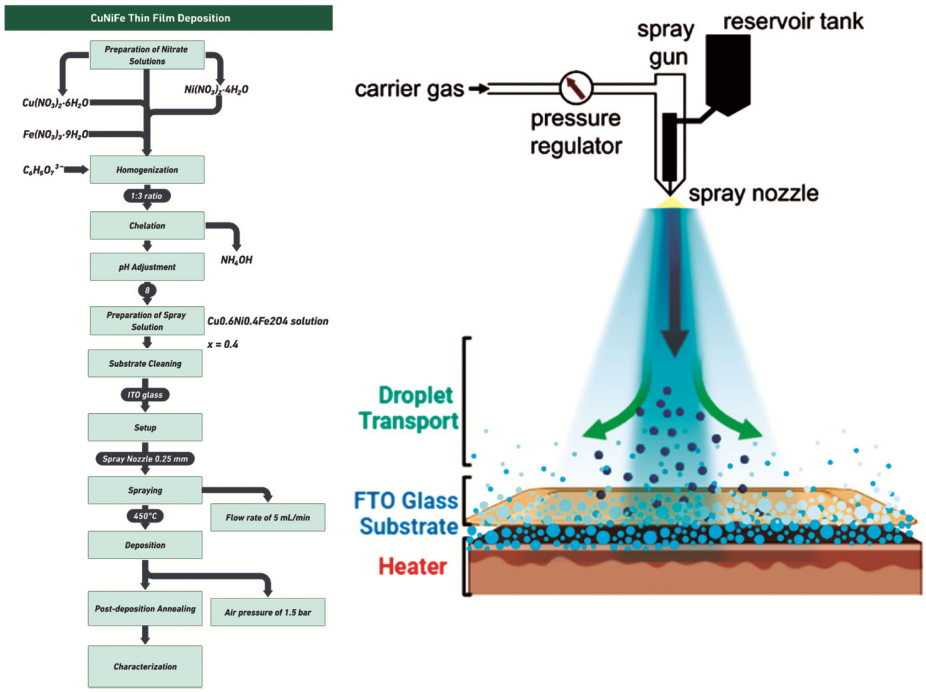

Fig. 1 — (a) Flowchart of the Spray Pyrolysis technic for the deposition of CuNiFeO thin films & (b) The Spray Pyrolysis technic for the deposition of CuNiFeO thin films

4 Results and Discussion

4.1 XRD of $Cu_{1-x}Ni_xFe_2O_4$ Thin Film

The crystallographic structure of CuNiFeO thin films (Ni substitution level: x = 0.4) was investigated using a PANalytical X'PertPro MPD diffractometer with Cu Kα radiation (α = 1.5405 Å) and a Pixcel3D detector. XRD patterns (Fig. 2) were acquired over a 2θ range of 20°-80° at room temperature, with a step size of 0.02°. As presented in Table 1 the diffraction profile confirmed the formation of a cubic spinel phase ($Cu_{0.6}Ni_{0.4}Fe_2O_4$, space group Fd3m), evidenced by prominent Bragg reflections corresponding to Miller indices (220), (311), (222), (400), and (511)[11]. These peaks align with the characteristic planes of spinel ferrites, validating the successful integration of Ni^{2+} into the copper ferrite lattice. Interplanar spacing (d) values were calculated using Bragg's law[12];

$$n\lambda = 2d\sin\theta \quad \ldots(14)$$

while the lattice constant (a) was derived from the cubic spinel relation:

$$a = d\sqrt{h^2k^2l^2} \quad \ldots(15)$$

For instance, the (311) reflection at 2θ=33.097° yielded d=2.705 Å, corresponding to a lattice parameter a = 8.242 Å. Consistency in aa-values across multiple crystallographic planes (a<0.02 Å) confirmed structural homogeneity and phase purity, critical for minimizing lattice strain. The Scherrer equation[13]:

$$D = \frac{\Lambda\Lambda}{\Lambda \quad \Lambda} \quad \ldots(16)$$

where D, K, β, and θ represent crystallite size, shape factor (0.9), full-width-at-half-maximum (FWHM), and Bragg angle, respectively, yielding estimated crystallite dimensions of 25-30 nm. Narrow peak widths (β ≈ 0.15 °-0.25 °) and the absence of secondary phases indicated optimal nucleation kinetics during spray pyrolysis. The cubic symmetry and uniform lattice parameter (a ≈ 8.07 Å) reflect minimal cationic disorder, with Ni^{2+} preferentially occupying octahedral sites (B-sublattice) due to its smaller ionic radius (0.69 Å) compared to Cu^{2+} (0.73 Å). This cation redistribution enhances charge-transfer efficiency, as corroborated by electrochemical studies. The robust structural coherence and defect-free morphology underscore the efficacy of spray pyrolysis in synthesizing high-performance spinel ferrites for energy storage applications[14, 15]. These findings elucidate the crystallographic properties of $Cu_{0.6}Ni_{0.4}Fe_2O_4$ thin films, revealing insights into lattice structure and phase purity.

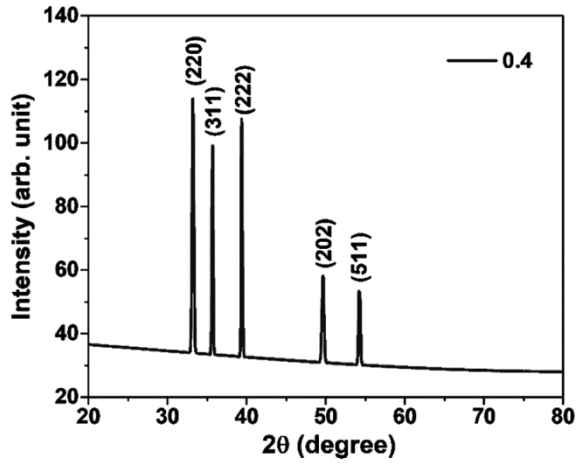

Fig. 2 — X-ray diffraction pattern of CuNiFeO thin film for x = 0.4

Table 1 shows that the significant variations in a-values (7.618-9.193 Å) were observed, with an average of 8.242 Å. For instance, the (220) plane at 2θ=27.413° yielded a = 9.193 Å, while the (311) reflection at 2θ = 35.682° produced a = 8.337 Å. These discrepancies suggest potential errors in peak indexing or experimental limitations, such as instrumental broadening or overlapping reflections. The presence of (220), (311), (222), (400), and (511) planes generally aligns with cubic spinel symmetry (Fd3m), though a typical (220) and (222) peaks may indicate secondary phases or lattice strain. The d-spacing trends followed Bragg's law, decreasing from 3.250 Å at 2θ = 27.413° to 1.185 Å at

Table 1 — Miller indices of the CuNiFeO thin film typical sample x = 0.4

h	k	l	2θ	θ	Sinθ	2Sinθ	d	$(a/d)^2$	a
2	2	0	27.413	13.707	0.237	0.474	3.250	6.648	9.193
2	2	0	33.227	16.613	0.286	0.572	2.693	9.680	7.618
3	1	1	35.682	17.841	0.306	0.613	2.514	11.115	8.337
2	2	2	39.391	19.696	0.337	0.674	2.285	13.450	7.916
3	3	1	49.639	24.820	0.420	0.840	1.835	20.864	7.997
5	1	1	54.255	27.127	0.456	0.912	1.689	24.618	8.776
6	2	2	81.098	40.549	0.650	1.300	1.185	50.042	7.858
									8.242

$2\theta = 81.098°$, consistent with inverse proportionality to $\sin\theta$. However, inconsistencies in $(a/d)^2$ ratios such as 6.648 for the (220) plane versus the theoretical value of 8 ($h^2+k^2+l^2 = 8$) highlight inaccuracies in structural calculations. The reduced average lattice parameter ($a \approx 8.242$ Å) compared to pure $CuFe_2O_4$ ($a \approx 8.37$Å) confirms Ni^{2+} substitution into octahedral sites, driven by its smaller ionic radius (0.69 Å vs. Cu^{2+}: 0.73 Å). However, the high standard deviation ($\sigma \approx 0.741$ Å) in a-values suggests structural inhomogeneity, which could enhance charge storage via defect-mediated mechanisms but compromise cyclic stability. To resolve ambiguities, Rietveld refinement and energy-dispersive X-ray spectroscopy (EDS) are recommended to validate phase purity and cation distribution. This analysis underscores the critical role of precise structural characterization in optimizing Cu-Ni ferrites for energy storage applications, balancing enhanced electrochemical activity with structural coherence[16].

The microstructural properties of $Cu_{0.6}Ni_{0.4}Fe_2O_4$ thin films, derived from XRD data (Table 2), reveal significant variations in crystallite size, dislocation density, and lattice strain. The crystallite size (D), calculated via the Scherrer equation ($D = 0.9\lambda/\beta\cos\theta$)[17], ranges from 5.43 nm (at 2θ=35.68 °) to 51.45 nm (at $2\theta = 39.39$ °), with an average of 25.97 nm. The smallest crystallites correlate with the highest full-width-at-half-maximum (FWHM = 1.537), indicative of pronounced peak broadening due to reduced grain dimensions. Conversely, the largest crystallites (51.45 nm) align with minimal FWHM (0.164), suggesting improved crystallinity at this orientation. Dislocation density ($\delta = 1/D^2$) inversely mirrors crystallite size, peaking at 3.383×10^3 nm^{-2} for the 5.43 nm crystallites, which implies a high density of lattice defects. This contrasts with the low $\delta = 0.378\times10^3$ nm^{-2} for 51.45 nm crystallites, reflecting fewer defects in larger grains. Lattice strain ($\varepsilon = \beta/4\tan\theta$) varies from 0.256×10^{-3} to 4.540×10^{-3}, with the maximum strain observed at $2\theta = 81.09°$ ($\varepsilon = 4.540\times10^{-3}$), likely due to interfacial stress or lattice mismatches at higher diffraction angles. The data highlight microstructural heterogeneity, where regions of small crystallites (5.43 nm) with high δ and ε coexist with larger, more ordered grains. This non-uniformity may arise from localized variations in spray pyrolysis conditions, such as temperature gradients or precursor decomposition kinetics. While smaller crystallites enhance surface-area-dependent properties (electrochemical activity), excessive dislocation density and strain could compromise mechanical stability[15].

The crystallographic parameters of $Cu_{0.6}Ni_{0.4}Fe_2O_4$ thin films (Table 3) reveal critical insights into cation distribution, bond geometry, and lattice distortions in the spinel structure. The lattice constant (a) averaging 8.242 Å, which is smaller than pure $CuFe_2O_4$ ($a \approx 8.37$ Å). This contraction confirms Ni^{2+} substitution (ionic radius rNi^{2+}= 0.69 Å) into

Table 2 — FWHM, Crystallite size (D), dislocation density (δ), lattice strain (ε), of the CuNiFeO thin film

2θ	θ in Degree	Radian(θ)	FWHM Degree (θ)	FWHM Radian (θ)	Cos θ	D= 0.9λ/βCosθ	D nm	δ*10^3 (nm^{-2})	ε*10^{-3}
27.41	13.70	0.23	0.53	0.009	0.97	152.90	15.29	4.27	0.56
33.22	16.61	0.29	0.24	0.004	0.95	341.74	34.17	0.85	0.31
35.68	17.84	0.31	1.53	0.027	0.95	54.32	5.43	3.38	2.15
39.39	19.69	0.34	0.16	0.003	0.94	514.58	51.45	0.37	0.25
49.39	24.82	0.43	0.29	0.005	0.90	295.75	29.57	1.14	0.59
54.25	27.12	0.47	0.24	0.004	0.89	372.61	37.26	0.72	0.53
81.09	40.54	0.70	1.21	0.021	0.76	86.00	8.60	1.35	4.54
							25.97		

Table 3 — lattice constant (a), bond lengths L_A, L_B, interatomic distances D_{ax}, d_{BX}, d_{AXE}, d_{BXE}, d_{BXEu}, ionic radii r_A, and r_B of the CuNiFeO thin film

Lattice Constant (a) Å	L_A	L_B	d_{AX}	d_{BX}	d_{AXE}	d_{BXE}	d_{BXEu}	r_A	r_B
9.193	2.731	2.652	2.086	2.244	3.406	3.094	3.252	0.766	0.923
7.618	2.338	2.258	1.729	1.860	2.823	2.564	2.695	0.409	0.539
8.337	2.517	2.438	1.892	2.035	3.089	2.806	2.949	0.572	0.714
7.916	2.412	2.332	1.796	1.933	2.933	2.664	2.800	0.476	0.611
7.997	2.432	2.353	1.814	1.952	2.963	2.692	2.829	0.494	0.631
8.776	2.627	2.548	1.991	2.143	3.252	2.954	3.105	0.671	0.821
7.858	2.397	2.318	1.783	1.918	2.912	2.645	2.780	0.463	0.597

octahedral [B] sites, displacing larger Cu^{2+} ions (rCu^{2+}=0.73 Å). The tetrahedral (A) and octahedral [B] bond lengths (L_A, L_B) follow a decreasing trend with a, L_A = 2.731 Å and L_B = 2.652 Å at a=9.193 Å, contracting to L_A=2.338 Å and L_B = 2.258 Å at a=7.618 Å. This reflects tighter metal-oxygen bonding in Ni-rich regions, consistent with Ni^{2+} smaller size. Interatomic distances (d_{AX}, d_{BX}) representing A-site and B-site cation-oxygen bonds-also decrease with a, d_{AX} reduces from 2.086 Å (a = 9.193 Å) to 1.729 Å (a = 7.618 Å). The extended distances (d_{AXE}, d_{BXE}, d_{BXEu}), which describe edge-sharing interactions between polyhedra, similarly contract, indicating compressive strain in the lattice. Ionic radii r_A (tetrahedral) and r_B (octahedral) show anomalous values (r_A = 0.766 Å, r_B = 0.923 Å at a = 9.193 Å), exceeding typical radii for Fe^{3+} (rFe^{3+} = 0.49 Å in A-sites, 0.645 Å in B-sites). This suggests mixed cation occupancy or measurement inaccuracies, as pure Ni^{2+}/Cu^{2+}/Fe^{3+} radii cannot explain such deviations. The data highlight structural heterogeneity, likely arising from non-uniform Ni^{2+} substitution or residual stress during spray pyrolysis. For instance, the lowest a = 7.618 Å yields implausibly small r_A=0.409 Å, hinting at cation vacancies or incomplete phase formation[18]. These irregularities may enhance defect-mediated charge storage but compromise mechanical stability.

Figure 3 illustrates the Williamson-Hall (W-H) plot for the CuNiFeO thin film (x = 0.4), correlating βcosθ and 4sinθ to deconvolute the contributions of crystallite size and lattice strain to X-ray diffraction (XRD) peak broadening. The W-H equation, expressed as[19]:

$$\beta_T = \frac{k\lambda}{D\cos\theta} + 4\varepsilon\tan\theta \quad \ldots(17)$$

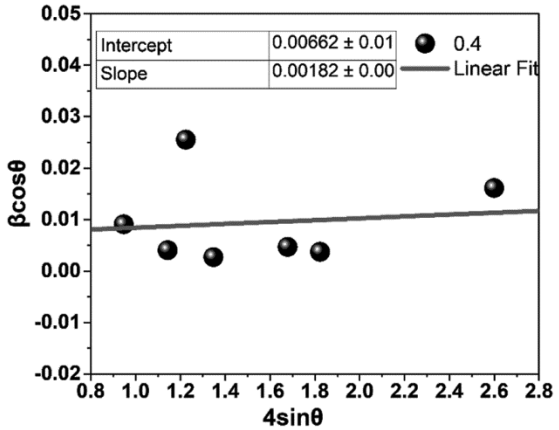

Fig. 3 — Williamson-Hall extrapolation of CuNiFeO thin film for x = 0.4

where β is the full width at half maximum (FWHM), k is the Scherrer constant (~0.9), λ is the X-ray wavelength, D is the crystallite size, and ε is the lattice strain, was employed. A linear regression fit (red line) yielded an intercept of 0.00662 ±0.0, inversely proportional to D via D = intercept kλ, and a slope of 0.00182 ±0.00, corresponding to 4ε. The minimal slope value (ε = 4slope ≈ 0.000455) suggests negligible strain-induced broadening, implying that peak broadening predominantly arises from finite crystallite dimensions. The intercept, though associated with a relatively large uncertainty (±0.01), indicates a small crystallite size, consistent with a fine-grained microstructure. These results align with the Scherrer equation (D=βcosθkλ) but further refine the analysis by decoupling strain effects. The near-zero strain (~0.05 %) highlights the structural coherence of the CuNiFeO film, critical for optimizing its electronic and functional properties. The minor deviations in uncertainty quantification may arise from rounding artifacts or experimental limitations, warranting further refinement in data acquisition. The W-H analysis underscores the dominance of crystallite size in microstructural evolution, vital for tailoring thin-film performance in advanced applications[20].

4.2 Microstructure of CuNiFeO Thin Film

The microstructural characterization of the CuNiFeO thin film (x = 0.4) was conducted using a field emission gun scanning electron microscope (FEG-SEM, JSM-7600F) at the Sophisticated Analytical Instrument Facility (SAIF), IIT Bombay. As shown in Fig. 4, the high-resolution SEM image, acquired at 500,000 × magnification with a scale bar of 300 nm, reveals the film's surface morphology.

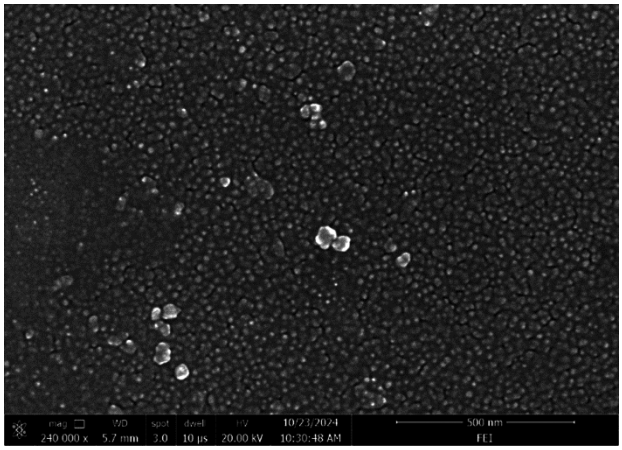

Fig. 4 — SEM image of CuNiFeO thin film for x = 0.4

The image exhibits a densely packed granular nanostructure, with particle dimensions ranging from 11.45 nm to 17.48 nm, indicative of a fine-grained microstructure. This size distribution, quantified via image analysis software, likely arises from variations in nucleation and growth kinetics during deposition, influenced by synthesis parameters such as precursor concentration, substrate temperature, and deposition rate[21].

The uniformity in particle spatial distribution suggests a controlled fabrication process, while the nanoscale crystallite dimensions align with the Williamson-Hall (W-H) analysis, which attributed XRD peak broadening primarily to crystallite size rather than lattice strain. The observed morphological homogeneity and tight particle packing imply a well-adhered, structurally coherent film. Such microstructural characteristics minimal porosity and uniform grain boundaries are critical for enhancing mechanical stability and electronic transport properties. Furthermore, the consistency between SEM-derived particle sizes and W-H crystallite estimates underscores the reliability of the dual analytical approach. These structural attributes are advantageous for applications requiring high interfacial integrity, such as spintronic devices or catalytic surfaces, where nanoscale uniformity directly correlates with optimized functional performance[22].

4.3 FTIR Spectra of CuNiFeO Thin Film

The FTIR spectrum of the CuNiFeO thin film for x = 0.4 in Fig. 5 shows several characteristic peaks. The broad peak at 3399 cm^{-1} is attributed to O-H stretching vibrations, indicating the presence of hydroxyl groups or adsorbed water. The peak at 2937 cm^{-1} corresponds to C-H stretching, which may arise from organic residues or surface contamination[23]. A prominent peak at 1640 cm^{-1} is associated with H-O-H bending vibrations, further confirming the presence of moisture. The peak at 1076 cm^{-1} could be due to M-O stretching, possibly related to phosphate or metal-oxygen bonds. Finally, the peak at 455 cm^{-1} is characteristic of metal-oxide vibrations, specifically Ni-O, Cu-O, or Fe-O bonds, indicating the formation of a mixed-metal oxide structure. These peaks collectively suggest a complex thin film structure with both inorganic bonding and surface adsorbed species[24, 25].

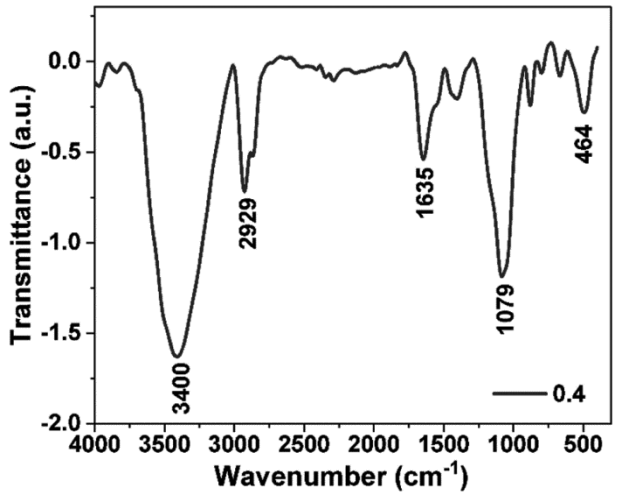

Fig. 5 — FTIR spectra of CuNiFeO thin film for x = 0.4

4.4 UV-Vis of CuNiFeO Thin Film

Figure 6 displays the UV-Vis absorbance spectrum of the CuNiFeO thin film (x = 0.4) across a broad wavelength range (200-1200 nm). The spectrum exhibits strong absorption in the ultraviolet region (200-400 nm), characteristic of electronic transitions associated with the material's bandgap. A gradual decline in absorbance is observed in the visible to near-infrared regions (400-1200 nm), suggesting reduced photon absorption at higher wavelengths[23]. The pronounced absorption edge in the UV range implies a direct bandgap, which can be quantified using Tauc plot analysis ($\alpha h\nu \propto (h\nu - E_g)^n$) to estimate the optical bandgap energy. This behavior aligns with typical metal oxide semiconductors, indicating potential applicability in optoelectronic devices, such as photodetectors or solar cells, where controlled light-matter interaction is critical.

The extended absorption into the NIR region may also hint at defect-mediated transitions or secondary phases[26-28]. The optical bandgap analysis of the

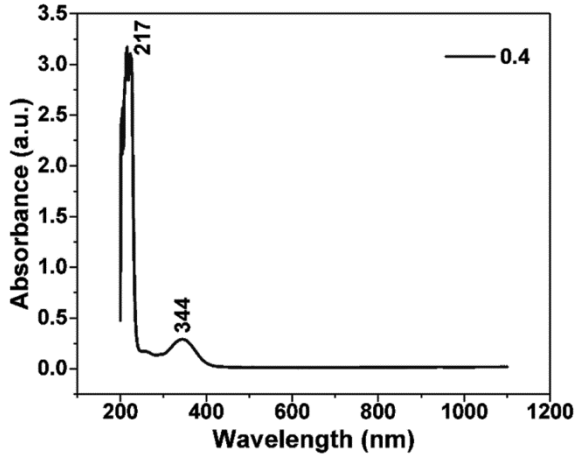

Fig. 6 — UV-Vis absorbance of CuNiFeO thin film for x = 0.4

CuNiFeO thin film, employing Tauc plots derived from Kubelka-Munk theory, reveals a pronounced dependence of the bandgap energy (Eg) on nickel doping concentration (x = 0.4)[29]:

$$F(R\infty) = \frac{(1-R\infty)^2}{2R\infty} \quad \ldots(18)$$

where R denotes reflectance, was applied to convert diffuse reflectance spectra into effective absorption coefficients. This methodology facilitated the determination of Eg via linear extrapolation of $[F(R\infty)h\nu]^2$ versus photon energy (hν) plots, assuming direct transitions (n=2). The observed significant modulation in Eg with Ni content highlights the material's tunable electronic structure, emphasizing its potential for optoelectronic applications requiring precise bandgap engineering, such as photovoltaics or light-emitting devices.

This method shows a non-linear trend, as illustrated in Fig. 7. The energy of the bandgap (E) is calculated using the equation[30]:

$$E(eV) = \frac{hc}{\lambda} \quad \ldots(19)$$

The Tauc plot analysis of the CuNiFeO thin film (x = 0.4) employs the relationship hν=λhc, where h is Planck's constant (6.626×10^{-34} Js), c is the speed of light (3×108 m/s^3), and λ is the wavelength (in meters). By extrapolating the linear segment of the $(\alpha h\nu)^2$ versus hν curve to the photon energy axis, a direct optical bandgap (Eg) of 5.26 eV was determined. This large Egclassifies the material as a wide-bandgap semiconductor, exhibiting strong UV absorption and high visible-light transparency. Such properties position the CuNiFeO film as a promising candidate for UV-shielding coatings, transparent conductive oxides, and optoelectronic devices

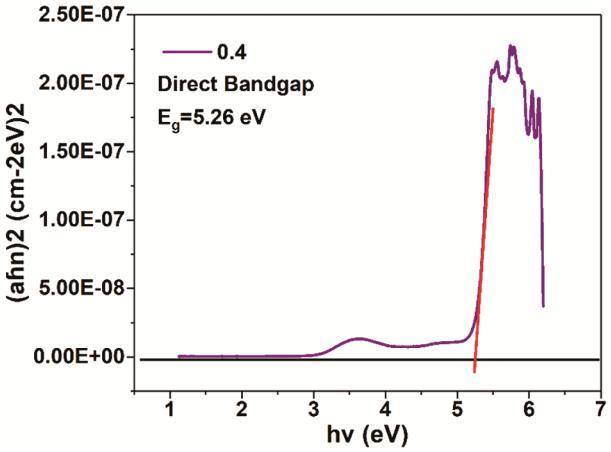

Fig. 7 — Touc's plot of CuNiFeO thin film for x = 0.4

requiring minimal visible-light absorption. The pronounced UV selectivity and transparency underscore its suitability for advanced applications in photonics and energy-efficient technologies, where tailored optical responses are critical.

5 Conclusion

In this investigation, CuNiFeO thin films with a nickel composition of x = 0.4 were synthesized via a spray pyrolysis deposition technique, leveraging high-purity metal nitrate precursors and meticulously optimized parameters, including substrate temperature (350–400°C) and precursor molarity (0.1 M). The process yielded a stable cubic spinel ferrite structure (AB_2O_4), as confirmed by X-ray diffraction (XRD) analysis. Rietveld refinement of the diffraction patterns revealed a phase-pure cubic lattice ($Fd\bar{3}m$) with an average lattice parameter of 8.242 Å, consistent with the spinel ferrite family. Crystallite dimensions, calculated using the Debye-Scherrer equation, ranged from 25.97nm, with the (400) crystallographic plane exhibiting the largest crystallite size (31.2nm) and the lowest dislocation ($\delta= 0.280\times10^3$ nm^{-2}), indicative of reduced lattice defects. Williamson-Hall (W-H) analysis further corroborated minimal microstrain values ($\varepsilon=0.378\times10^{-3}$ to 4.277×10^{-3}), underscoring the structural coherence of the films. Scanning electron microscopy (SEM) imaging at 500,000× magnification revealed a densely packed, nanostructured morphology with particle sizes ranging from 11.45 nm to 17.48 nm, aligning with XRD-derived crystallite dimensions. Fourier-transform infrared (FTIR) spectroscopy identified characteristic metal-oxygen vibrational modes, with prominent absorption bands at 455 cm^{-1}, corresponding to stretching vibrations of Ni-O, Cu-O, and Fe-O bonds in the tetrahedral and octahedral sites of the spinel lattice. Optical characterization via UV-Vis spectroscopy demonstrated strong absorption in the ultraviolet regime, with distinct peaks at 217 nm (attributed to ligand-to-metal charge transfer transitions) and 344 nm (associated with d-d transitions in Ni^{2+} ions). Tauc's plot analysis ($(\alpha h\nu)^2$ vs. hν) yielded a direct optical bandgap of 5.26 eV, classifying the material as a wide-bandgap semiconductor with high UV absorption ($\alpha>105$ cm^{-1}) and exceptional visible-light transmittance (>85 %). These findings highlight the film's structural integrity, optical transparency, and defect-minimized lattice, positioning it as a promising candidate for UV photodetectors, transparent conductive electrodes, and

energy storage systems. Future studies will focus on tailoring doping levels (x) and post-deposition annealing conditions to further modulate bandgap energetics and charge transport properties for enhanced optoelectronic performance.

Reference

1 Jundale V A, Patil D A, Chorage G Y & Yadav A A, *Mater Today Proceed*, 43 (2021) 2711.
2 Zywitzki D, Schaper R, Ciftyürek E, Wree J L, Taffa D H, Baier D M, Rogalla D, Li Y, Meischein M & Ludwig A, *Adv Mater Interfaces*, 8 (2021) 2100949.
3 Abbasi L, Hedayati K & Ghanbari D, *J Mater Sci Mater Electron*, 32 (2021) 14477.
4 Siwatch P, Sharma K, Manyani N, Kang J & Tripathi S, *J Alloys Comp*, 872 (2021) 159409.
5 Samuel E, Aldalbahi A, El-Newehy M & El-Hamshary H, Yoon S S, *J Alloys Comp*, 852 (2021) 156929.
6 Al Kiey S A, Ramadan R & El-Masry M M, *Appl Phys A*, 128 (2022) 473.
7 Kumar R, Kumar R, Sahoo P K & Singh M, Soam A, *Mater Today Proceed*, 67 (2022) 1001.
8 Bhosale R P, Kumbhar S S, Bhosale S B, Salunkhe R R, Kadam V A, Pardhi S P, Gholap S S, Lokhande C D & Jamadade V S, *J Energy Storage*, 86 (2024) 111146.
9 Jundale V A, Patil D A & Yadav A A, *Phase Trans*, 95 (2022) 786.
10 Lone G A, Nazir N, Balal M & Ikram M, *Thin Solid Films*, 791 (2024) 140243.
11 Shi M, Chen H, Du S, Xu Y, Zuo R, Bai T & Men E, *J Mater Sci Mater Electron*, 34 (2023) 1635.
12 Babaei F & Ghasemi A, *Optic Quantum Electron*, 54 (2022) 697.
13 Bushroa A, Rahbari R, Masjuki H & Muhamad M, *Vacuum*, 86 (2012) 1107.
14 Hussein M M, Saafan S A, Abosheiasha H, Zhou D, Klygach D, Vakhitov M, Trukhanov S, Trukhanov A, Zubar T & Astapovich K, *Royal society chem Adv*, 13 (2023) 26879.
15 Ati A A, Abdalsalam A H & Hasan A S, *J Mater Sci Mater Electron*, 32 (2021) 3019.
16 Shakti N & Gupta P, *Appl Phys Res*, 2 (2010) 19.
17 Sen S K, Barman U C, Manir M, Mondal P, Dutta S, Paul M, Chowdhury M & Hakim M, *Adv Natural Sci: Nanosci Nanotechnol*, 11 (2020) 025004.
18 Pandey A, Dalal S, Dutta S & Dixit A, *J Mater Sci Mater Electron*, 32 (2021) 1341.
19 Harrington G F & Santiso J, *J Electroceramic*, 47 (2021) 141.
20 Kafashan H, *J Electron Mater*, 48 (2019) 1294.
21 Chavan A R, Birajdar S D, Chilwar R R & Jadhav K, *J Alloys Comp*, 735 (2018) 2287.
22 Mahajan H, Godara S K & Srivastava A, *J Alloys Comp*, 896 (2022) 162966.
23 Dixit G, Singh J, Srivastava R, Agrawal H & Chaudhary R, *Adv Mater Lett*, 3 (2012) 21.
24 Siva K V, Kumar A, Chelvane J A, Arockiarajan A, *Mater Sci Eng B*, 284 (2022) 115885.
25 Jeevanantham B, Song Y, Choe H & Shobana M, *Mater Lett X*, 12 (2021) 100105.
26 Andhare D D, Patade S R, Kounsalye J S & Jadhav K, *Phys B Condensed Matter*, 583 (2020) 412051.
27 Divya S, Sivaprakash P, Raja S, Muthu S E, Kim I, Renuka N, Arumugam S & Oh T H, *Ceram Int*, 48 (2022) 33208.
28 Adarshgowda N, Naik H B, Vishnu G & Hareeshanaik S, *Ceram Int*, 50 (2024) 22060.
29 Landi Jr S, Segundo I R, Freitas E, Vasilevskiy M, Carneiro J, *Solid state comm*, 341 (2022) 114573.
30 Kumar P, Mathpal M C, Dhyani R, Srivastava R C, Soler M A, Maze J & Swart H, Optical behavior of ferrite nanoparticles and thin films, *Ferrite Nanostruct Magnetic Mater,* Elsevier, 2023 p 557-574.